Recurrent Inhibitory Dynamics: The Role of State-Dependent Distributions of Conduction Delay Times

CHRISTIAN W. EURICH*, MICHAEL C. MACKEY†‡ AND HELMUT SCHWEGLER*

*Institute of Theoretical Physics, University of Bremen, Fachbereich 1, NW 1, P.O. Box 330 440, D-28334 Bremen, Germany and † Departments of Physiology, Physics, & Mathematics, Centre for Nonlinear Dynamics, McGill University, Montreal, Canada

We have formulated and analysed a dynamic model for recurrent inhibition that takes into account the state dependence of the delayed feedback signal (due to the variation in threshold of fibres with their size) and the distribution of these delays (due to the distribution of fibre diameters in the feedback pathway). Using a combination of analytic and numerical tools, we have analysed the behaviour of this model. Depending on the parameter values chosen, as well as the initial preparation of the system, there may be a spectrum of post-synaptic firing dynamics ranging from stable constant values through periodic bursting (limit cycle) behaviour and chaotic firing as well as bistable behaviours. Using detailed parameter estimation for a physiologically motivated example (the CA3-basket cell-mossy fibre system in the hippocampus), we present some of these numerical behaviours. The numerical results corroborate the results of the analytic characterization of the solutions. Namely, for some parameter values the model has a single stable steady state while for the others there is a bistability in which the eventual behaviour depends on the magnitude of stimulation (the initial function).

1. Introduction

Recurrent inhibition, in which activity in a population of neurons excites a second population that, in turn, inhibits the activity of the first, is ubiquitous throughout the nervous systems of species ranging from insects through the mammals. The widespread occurrence of recurrent inhibition has intrigued many investigators, and generated considerable speculation concerning its functional significance.

‡ Author to whom correspondence should be addressed. 3655 Drummond Street, Room 1124, Montreal, Quebec, Canada H3G 1Y6.
E-mail: mackey@cnd.mcgill.ca

Time delays are ubiquitous in the functioning of biological systems, and the nervous system is no exception. In the nervous system, delays occur at the synaptic level due to transmitter release dynamics and the integration time of inhibitory and excitatory post-synaptic potentials (IPSPs and EPSPs) at the dendritic tree level where post-synaptic potentials (PSPs) have a finite conduction time to the soma, and in the axons due to the finite axonal conduction speed of action potentials (Ermentrout & Kopell, 1998; Ernst *et al.*, 1995; Eurich *et al.*, 1999, 2000).

When delays are merely involved in the transmission of information along a feed forward pathway, their effect is to give rise to

dispersion of signals that may have been initially quite synchronous and to affect the timing of these signals from diverse sources. (An exception are systems where the timing of signals is important. In such cases, conduction delays are adapted to certain tasks. Examples include sound localization in barn owls (Carr & Konishi, 1990) and the transmission of visual information by retinal ganglion cells of the cat (Stanford, 1987).) When these physiologically derived delays are part of feedback pathways (like recurrent excitatory and/or recurrent inhibitory circuits), then the presence of the delays can have profound functional effects. The dynamic consequences of these delays in feedback situations have rarely been considered in the context of neural dynamics.

The ubiquitous nature of recurrent inhibition has generated a plethora of mathematical models, but all have failed to include some of the relevant neurophysiological detail. In this paper, we extend a previous model for recurrent inhibition to include:

• The distribution of delays in the recurrent inhibitory pathway due to the distribution of fibre diameters in the feedback pathway.
• The variation in the sizes of recurrent fibres excited as a consequence of the variation in threshold with fibre size.

These two facts, neglected in all previous models of recurrent inhibition, lead to an interesting mathematical problem since they imply a *state-dependent distribution of delays*. Through an analysis of this problem, we have studied the dynamical effects of this neurophysiologically based state dependent delay.

This paper is organized as follows. In Section 2, we briefly survey previous models for recurrent inhibition before starting the development of an extension of the model of Mackey & an der Heiden (1984) to include state-dependent distributions of delays. Section 2.1 details how we have determined the nature of the state-dependent distribution of feedback conduction delays. The basic dynamics of the membrane potentials V are developed in Section 2.2, as is the relation between membrane potential and neural firing frequency. The model is reduced to a dimensionless form in Section 2.3. Section 3 summarizes

the numerical and analytic results of our analysis of the model, the full details of which are in Appendix A. (The steady states are considered in Appendix A.1, and their local stability in Appendix A.2.) In Section 4, we consider a specific realization of our model based on the hippocampal mossy fibre-CA3 pyramidal cell-basket cell complex. Parameter estimation for the model of Section 2 is carried out in Section 4.1, and the numerical behaviour of the model is explored in Section 4.2. We conclude with a brief discussion in Section 5.

2. Model Development

Many authors have considered mathematical models for recurrent inhibitory processes (an der Heiden & Mackey, 1987; an der Heiden *et al.*, 1981; Castelfranco & Stech, 1987; Martinez & Segundo, 1983; Milton, 1996; Guevara *et al.*, 1983; Mackey & an der Heiden, 1984; Milton *et al.*, 1989, 1990; Plant, 1981; Traub & Miles, 1991; Traub *et al.*, 1991, 1993, 1994, 1996, 1999a, b; Traub & Bibbig, 2000; Tuckwell, 1978; Wilson & Cowan, 1972, 1973). Comprehensive surveys can be found in an der Heiden (1979, 1991) and Milton (1996).

These previous modelling efforts span a range of complexity. Some include the barest of neurophysiological detail. Others include sophisticated assumptions concerning the synaptic transmission properties of the neural populations involved, as well as quite detailed assumptions concerning the underlying ionic processes leading to excitation in the postsynaptic population of excitatory neurons and the recurrent inhibitory population.

The model of Mackey & an der Heiden (1984) was intermediate in this range as the focus was on the dynamics effects of recurrent inhibition *per se*. That model considered the nonlinear feedback due to the stoichiometry of the inhibitory receptor interactions, the nonlinearities induced by the firing frequency vs. input relation, and the inherent delays induced by the recurrent feedback pathway. It was a natural consequence of the underlying physiology that the solutions showed a range of dynamic behaviour ranging from quiescence through regular, synchronized, oscillatory bursting
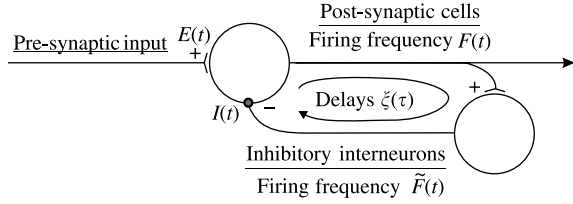
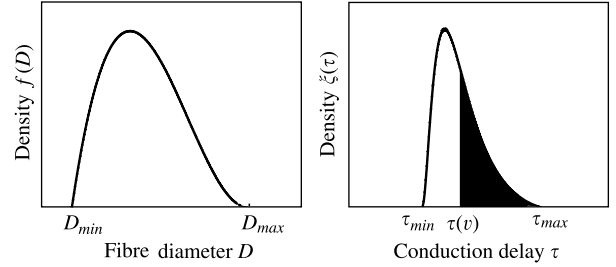FIG. 1. A diagrammatic representation of the inhibitory feedback loop. For mathematical notation, see text.

FIG. 2. A schematic representation of the density $f(D)$ of fibre diameters, and the corresponding density of delay times $\xi(\tau)$ as given in eqn (7). In the right-hand panel, increases in the post-synaptic potential V move the left-hand boundary toward τ_{min}, so for very large inputs V the entire density is involved.

behaviour to culminate in quite irregular firing behaviour of the excitatory cells. Additionally, the model displayed the property of *multi-stability* whereby the eventual solution behaviour could be highly dependent on the initial function that was chosen for the system (cf. an der Heiden & Mackey, 1982).

Here, as in Mackey & an der Heiden (1984), the important dependent variables will be the excitatory potential E in the excitatory population in response to stimulation of the pre-synaptic population, and the inhibitory potential I in the excitatory population due to the activation of the inhibitory interneurons. The difference between these two quantities, $E - I$, is the intracellular potential V (relative to the resting potential) and will be identified with the *input* of the excitatory population. The degree to which $V = E - I$ exceeds the post-synaptic threshold for activation (Θ) determines the firing properties of the excitatory population. Figure 1 shows a schematic representation of the feedback loop under consideration.

2.1. THE DISTRIBUTION OF CONDUCTION DELAY TIMES IS STATE DEPENDENT

One of the interesting aspects of this problem is that the inhibitory interneuron firing frequency $\tilde{F}(t)$ is related to the delayed excitatory cell firing frequency $F(t - \tau)$ weighted by the density ξ of the distribution of conduction delays (see Fig. 1). To see why this is so, consider the following.

It is well known (Jack *et al.*, 1975) that action potentials propagate with a conduction velocity which is an increasing function of the fibre diameter, and that this diameter dependence is different for myelinated and non-myelinated axons. Thus, if a single fibre in our feedback

pathway has a diameter D, then that fibre will have a conduction velocity (v) along the feedback pathway given by

$$v(D) = \chi D^b, \qquad (1)$$

where

$$b = \begin{cases} \frac{1}{2} & \text{for non-myelinated fibres,} \\ 1 & \text{for myelinated fibres.} \end{cases} \qquad (2)$$

If the feedback pathway has an effective length of L, then a fibre of diameter D will have a feedback conduction delay (τ) given by

$$\tau(D) = \frac{L}{v(D)} = \frac{L}{\chi D^b}. \qquad (3)$$

Assume now that the feedback pathway consists of a number of fibres distributed (with respect to their diameter) with a density $f(D)$ that is supported on the interval $[D_{min}, D_{max}]$ (see Fig. 2) where D_{min} and D_{max} are the minimal and maximal fibre diameters to be found in the recurrent pathway. To find the density $g(\tau)$ of the distribution of delays corresponding to the distribution of diameters remember simply that if a variable D is distributed with a density $f(D)$, then a transformation $\tau = h(D)$ of that variable will be distributed with a density

$$g(\tau) = f(h^{-1}(\tau)) \left| \frac{\mathrm{d} h^{-1}(\tau)}{\mathrm{d}\tau} \right|. \qquad (4)$$

In our case, $D = h^{-1} = (L/\chi\tau)^{1/b}$ so

$$g(\tau) = \frac{1}{b\tau}\left(\frac{L}{\chi\tau}\right)^{1/b} f\left(\left(\frac{L}{\chi\tau}\right)^{1/b}\right) \quad (5)$$

or

$$g(\tau) = \begin{cases} \dfrac{2}{\tau}\left(\dfrac{L}{\chi_n\tau}\right)^2 f\left(\dfrac{L^2}{\chi_n^2\tau^2}\right) & \\ \quad \text{non-myelinated fibres,} & \\ \dfrac{L}{\chi_m\tau^2} f\left(\dfrac{L}{\chi_m\tau}\right) & \\ \quad \text{for myelinated fibres.} & \end{cases} \quad (6)$$

From these considerations, it is clear that the density of the distribution of delay times $[\xi(\tau)]$ when the full feedback pathway is activated is given by

$$\xi(\tau) = \begin{cases} 0 & 0 \leqslant \tau < \tau_{min}, \\ g(\tau) & \tau_{min} \leqslant \tau \leqslant \tau_{max}, \\ 0 & \tau_{max} < \tau < \infty. \end{cases} \quad (7)$$

$\xi(\tau)$ is shown schematically in Fig. 2. Since $\xi(\tau)$ is a density,

$$\int_0^\infty \xi(\tau)\,\mathrm{d}\tau = 1. \quad (8)$$

The second interesting aspect of this problem is that the density of the distribution of conduction delay times that we have just determined is in fact dependent on the state of the system. Consider the following.

As Jack *et al.* (1975) have pointed out, the threshold Θ for the intracellular activation of a nerve fibre of diameter D must be proportional to $D^{3/2}$. This has the following interesting consequences:

- Small cells in the feedback pathway (which have the largest conduction delays) have a low threshold for activation; while
- Large cells in the feedback pathway (with short conduction delays) will have a large threshold for activation.

Thus if $\Theta \sim D^{3/2}$ then $\Theta \sim \tau^{-3/2b}$ or $\Theta = \Theta_0\tau^{-3/2b}$ and

$$\Theta(\tau) = \Theta_0 \begin{cases} \tau^{-3} & \text{for non-myelinated fibres,} \\ \tau^{-3/2} & \text{for myelinated fibres.} \end{cases} \quad (9)$$

The logical consequence of these facts is that the density of the distribution of conduction delay times that we have developed will in fact depend on the level of activity in the population, i.e. it will be *state dependent*. This state dependence will manifest itself in the following way. At very low levels of input $V = E - I$ to the excitatory population, we will find that the distribution of delay times is narrowly focused on a small interval of delays $[\underline{\tau}(V), \tau_{max}]$, where $\underline{\tau}(V)$ is given by

$$\underline{\tau}(V) = \left(\frac{\Theta_0}{V}\right)^{2b/3}. \quad (10)$$

As the input $E - I$ is progressively increased, the minimum of the support interval $[\underline{\tau}(V), \tau_{max}]$ will progressively decrease until, with maximal input, we will finally have the density of the conduction time delays supported on $[\tau_{min}, \tau_{max}]$. Thus, it is clear that with progressively increasing input $V = E - I$ we have a state-dependent minimal delay, $\underline{\tau}(V)$. When the population of cells is not fully activated, this leads to a state-dependent density of the distribution of delay times, see Fig. 2.

2.2. DYNAMICS OF THE INHIBITORY AND EXCITATORY POTENTIALS

In the presence of constant pre-synaptic excitatory drive E (mV), the dynamics in the model with a distribution of delays (not including the state dependence) are governed by an equation of the form

$$\frac{\mathrm{d}I}{\mathrm{d}t} = -\gamma I + \tilde{F}\eta(\tilde{F}), \quad (11)$$

where I (mV) is the inhibitory potential due to the recurrent feedback, $\tilde{F}$ (s^{-1}) is the instantaneous inhibitory interneuron firing frequency, γ (s^{-1}) is the inverse of the membrane time constant for the decay of inhibition, and η is a frequency-dependent interaction coefficient (an der Heiden and Mackey, 1982) that is a function of $\tilde{F}$. Writing dynamics (11) in terms of the intracellular potential V we have

$$\frac{\mathrm{d}V}{\mathrm{d}t} = -\frac{\mathrm{d}I}{\mathrm{d}t} = \gamma(E - V) - \tilde{F}\eta(\tilde{F}). \quad (12)$$

It is through the function η that the stoichiometry and the nonlinearity of the inhibitory feedback enter the problem. Specifically, η is given by

$$\eta(\tilde{F}) = R\Delta G(\tilde{F}). \qquad (13)$$

In eqn (13), R is the average number of inhibitory receptors per excitatory cell, and Δ is the magnitude (in mV) of the inhibitory post-synaptic potential resulting from the activation of one receptor. The *fraction* of inhibitory receptors *available* for activation is given by $G(\tilde{F})$.

To determine $G(\tilde{F})$ we must consider the stoichiometry of the inhibitory transmitter–receptor interaction. Of the total receptor population R, we assume that L are active (that is, combined with transmitter) and that M are inactive. We assume further that the transmitter–receptor interaction is governed by

$$M + nC \rightleftharpoons L, \qquad (14)$$

where n is the number of molecules of transmitter (C) required to activate one inhibitory receptor. Under the assumption that reaction (14) is sufficiently rapid to be at equilibrium, and that there is conservation of receptors so $R = L + M$, then it is straightforward to show that the fraction of receptors available for activation is given by

$$G(C) = \frac{K}{K + [C]^n}, \qquad (15)$$

where K [in units of $(\mu M\,L^{-1})^n$] is the equilibrium constant for eqn (14) and $[C]$ denotes the concentration (in units of $\mu M\,L^{-1}$) of inhibitory transmitter.

Taking this development further, we assume that the interneuronal intracellular pool of inhibitory transmitter is sufficiently large not to be depleted by the interneuronal activity. Then the relation between the released transmitter concentration $[C]$ and the firing frequency $\tilde{F}$ at the synaptic terminals of the interneuron will be given by $[C] = m\tilde{F}$, where m is a proportionality constant. Thus the function $G(\tilde{F})$ takes the final form

$$G(\tilde{F}) = \frac{K}{K + (m\tilde{F})^n}. \qquad (16)$$

To close this set of equations we must relate the instantaneous firing frequency $F(t)$ (the excitatory cell output) to the excitatory cell input $V = E - I$. To do this the following considerations are important.

Let $\Theta(\tau)$ be the threshold for the generation of an action potential in a fibre with a delay time τ as in eqn (9). Then we approximate the firing frequency at the soma of the excitatory cell by

$$F(V, \tau) = \kappa(V - \Theta(\tau))H(V - \Theta(\tau)), \qquad (17)$$

where κ has the dimensions of $Hz\,mV^{-1}$ and H is the Heavyside step function,

$$H(x) = \begin{cases} 0 & x < 0, \\ 1 & 0 \leqslant x. \end{cases} \qquad (18)$$

Since $F(V(t), \tau)$ is the firing frequency at the soma of the excitatory cell, the inhibitory interneuron firing frequency $\tilde{F}(t)$ will be $\alpha F(V(t - \tau), \tau)$ (α is a proportionality constant determined by the average number of action potentials in the excitatory cell required to elicit one action potential in the inhibitory interneuron) weighted by the distribution ξ of conduction delays. $\tilde{F}(t)$ is given explicitly by

$$\tilde{F}(t) = \alpha\kappa \int_0^\infty [V(t - \tau) - \Theta(\tau)]$$
$$\times H(V(t - \tau) - \Theta(\tau))\xi(\tau)\,d\tau. \qquad (19)$$

If we combine eqns (12), (13) and (16) into a single equation for the dynamics of the membrane potential we obtain

$$\frac{dV}{dt} = -\frac{dI}{dt} = \gamma(E - V) - \tilde{F}R\Delta\frac{K}{K + (m\tilde{F})^n}. \qquad (20)$$

To completely specify the semi-dynamical system described by eqns (19) and (20) we must additionally have an initial function

$$I(t') \equiv \varphi(t') \quad \text{for } t' \in (-\infty, 0]. \qquad (21)$$

2.3. DIMENSIONLESS FORM OF THE MODEL

To facilitate our later analysis of the model, as well as our numerical investigation, it is prudent to reduce the number of parameters in the model formulation through judicious scaling.

We start by scaling the temporal variables to the minimal delay τ_{min} and defining

$$\bar{t} = \frac{t}{\tau_{min}} \quad \text{and} \quad T = \frac{\tau}{\tau_{min}}. \qquad (22)$$

If we define the maximal threshold by $\Theta_{max} = \Theta(\tau_{min}) = \Theta\tau_{min}^{-3/2b}$ then we can scale all of the potentials to Θ_{max} using

$$\theta = \frac{\Theta}{\Theta_{max}}, \quad e = \frac{E}{\Theta_{max}}, \quad i = \frac{I}{\Theta_{max}}$$

$$\text{and} \quad v = \frac{V}{\Theta_{max}}. \qquad (23)$$

We further define two dimensionless firing frequencies by

$$f = \frac{F\tau_{min}}{\psi} \quad \text{and} \quad f_0 = \alpha\frac{\kappa\Theta_{max}\tau_{min}}{\psi}, \quad (24)$$

wherein the constant ψ is defined by

$$\psi^n = K\left(\frac{\tau_{min}}{m}\right)^n. \qquad (25)$$

Finally, we define two parameters Γ and β through

$$\Gamma = \gamma\tau_{min} \quad \text{and} \quad \beta = \frac{R\psi\Delta}{\Theta_{max}}. \qquad (26)$$

With these definitions, we can write eqn (20) in the dimensionless form

$$\frac{dv}{d\bar{t}} = \Gamma(e - v) - \beta\tilde{f}\frac{1}{1 + \tilde{f}^n} = \Gamma(e - v) - \beta\mathcal{G}(\tilde{f}),$$
$$(27)$$

wherein

$$\mathcal{G}(\tilde{f}) = \frac{\tilde{f}}{1 + \tilde{f}^n}. \qquad (28)$$

$\tilde{f}$ is given from eqn (19) by

$$\tilde{f}(v) = f_0 \int_0^\infty [v_T - \theta(T)]H(v_T - \theta(T))\bar{\xi}(T)\,dT$$
$$(29)$$

with

$$\theta(T) = T^{-3/2b}. \qquad (30)$$

In eqn (29) the notation v_T means

$$v_T(\bar{t}) \equiv v(\bar{t} - T)$$

and

$$\bar{\xi}(T) = \tau_{min}\xi(T\tau_{min}). \qquad (31)$$

3. Summary of Analytic and Numerical Model Properties

We have presented our full analytic analysis of the steady states of the model defined by eqns (19) and (20) in Appendix A, and the reader interested in the details may find them there. In this section, we merely give a brief resume of those results which are easy to state if difficult to demonstrate.

In terms of steady states, the results of Appendix A.1 show that, depending on the parameters of the model, there may be one, two, or three steady-state values of the membrane potential (cf. Fig. 7). We denote these by $vi, i = 1, 2, 3$ with $0 \leqslant v_*^1 \leqslant v_*^2 \leqslant v_*^3$. Since the firing frequency $\mathcal{F}(v_*)$ is a monotone function of v_* we therefore know that $\mathcal{F}(v_*^1) \leqslant \mathcal{F}(v_*^2) \leqslant \mathcal{F}(v_*^3)$. If a steady state $v_* \leqslant \theta_{min}$ there is no firing and $\mathcal{F}(v_*) = 0$.

From a point of view of stability, and thus what is likely to be observable either numerically or experimentally, we must rely on Appendix A.2 and Proposition 2. From these we know that regardless of the number of steady states v_*^1 may be either stable or unstable (if it is unstable it is replaced by an apparently stable limit cycle), v_*^2 is always unstable (and therefore will never be observed), and v_*^3 is always stable.

From an experimental and dynamical point of view perhaps the most interesting situation is that for which there are three coexisting steady states $0 \leqslant v_*^1 \leqslant v_*^2 \leqslant v_*^3$. In this case, there will be genuine bistable behaviour possible in which, depending on the initial function selected [cf. eqn (21)], the model behaviour will either go to a relatively high firing rate $\mathcal{F}(v_*^3)$ that will be constant in time, or there will be a lower firing rate $\mathcal{F}(v_*^1) \leqslant \mathcal{F}(v_*^3)$. This lower firing rate $\mathcal{F}(v_*^1)$ may be either stable (and constant), or unstable and periodic (and thus display bursting behaviour).

An extensive numerical investigation of the model defined by the dimensionless eqns (27)–(30) has been carried out. Briefly, we have found that in addition to the stable steady states, limit cycles, and bistability uncovered by the analytic analysis of Appendix A there can also be a hierarchy of bifurcations to limit cycles of higher period as well as solution behaviours that are apparently "chaotic". We have not presented these results here since the dimensionality of the parameter space that had to be searched is so high [the dimensionality is six, corresponding to the dimensionless parameters Γ, β, n, f_0, b and e in addition to the parameters defining the dimensionless distribution of delays $\bar{\xi}(T)$]. Rather, in the next section we pick recurrent inhibition in the hippocampus as a particular physiological example to localize a region in this high dimensional parameter space and then present numerical results for that situation.

4. A Particular Example

There are six parameters in the dimensionless model of Section 2.3. To localize attention to a smaller volume of the model parameter space, we have determined parameters for our recurrent inhibitory model using the hippocampal mossy fibre-CA3 pyramidal cell-basket cell complex as an example. In this case, the mossy fibres correspond to the pre-synaptic population, the CA3 pyramidal cells are the post-synaptic cells, the basket cells are the interneurons, and the inhibitory transmitter is GABA.

Thanks to the long-term efforts of Traub and his co-workers (Traub & Miles, 1991; Traub et al., 1991, 1993, 1994, 1996, 1999a, b; Traub & Bibbig, 2000) we have extremely detailed knowledge of the dynamics of the hippocampus that has been incorporated into sophisticated mathematical models of the hippocampal physiology. In estimating parameters for our model for the dynamics of recurrent inhibition based on hippocampal physiology, we fully realize that our model of recurrent inhibition lacks much of the physiological detail that these other models have. However, we are merely concerned with using the hippocampal data to derive physiologically realistic parameter values with which we

can explore the numerical behaviour of the model.

We first estimate the model parameters using a variety of hippocampal data in Section 4.1 and then present numerical results of our simulations in Section 4.2.

4.1. PARAMETER ESTIMATION

There are a number of parameters that must be estimated before the dimensionless parameters f_0, Γ and β can be determined and a coherent numerical investigation of the system defined by eqns (27)–(29) carried out. This section is devoted to an explanation of how we carried out this determination for the parameters that we were able to calculate from hippocampal experimental data. Our final determinations are summarized in Table 1.

• γ is the inverse of the time constant for the decay of inhibitory potentials. However, there are two types of inhibitory synapses mediated by GABA (Traub & Miles, 1991). The $GABA_A$ synapses have inhibitory currents carried by Cl^-, are located on the soma and apical dendrites, are blocked by penicillin, and have an associated membrane time constant of about 23 ms. The $GABA_B$ synapses mediate inhibitory currents carried by K^+, are located more distally on the dendrites, and are characterized by a long time constant of about 185 ms. Since the shorter time constant will dominate the decay of the inhibitory potentials we have taken $\gamma = (23\,\text{ms})^{-1} = 4.3 \times 10^{-2}\,\text{ms}^{-1}$.

• Δ is the size of the unitary IPSP that can be elicited in a pyramidal cell. From the data of Traub & Miles (1991, Fig. 3.2) this ranges between 0.5 and 1.5 mV. We have chosen $\Delta = 1\,\text{mV}$.

• R is the average number of GABA receptors per pyramidal cell. The direct estimates of Megías et al. (2001) place the average number of inhibitory synapses on CA1 pyramidal cells at 1700.

• K is the equilibrium binding constant between the inhibitory transmitter GABA and the excitatory cell GABA receptor. From cell culture preparations, this was determined in Nowak et al. (1982) to be $K = (5\,\mu\text{M})^3$.

TABLE 1

Parameters estimated for the hippocampal CA3 pyramidal cell-basket cell-mossy fibre inhibitory recurrent network

Parameter	Units	Hippocampal value	Reference
γ	ms^{-1}	4.3×10^{-2}	Traub & Miles (1991)
Δ	mV	1	Traub & Miles (1991)
R	—	~ 1700	Anderson *et al.* (1964), Traub & Miles (1991), Megías *et al.* (2001)
K	$(\mu M)^n$	$5^3 = 125$	Nowak *et al.* (1982)
m	$\mu M \, s$	0.62	See text
n	—	3	Nowak *et al.* (1982), Werman (1979)
α	—	0.4	Traub & Miles (1991)
κ	$(mV \, s)^{-1}$	20	Kandel & Spencer (1961)
τ_{min}	ms	5.6	Anderson *et al.* (1964)
τ_{max}	ms	9.1	Anderson *et al.* (1964)
Θ_{min}	mV	2	Kandel & Spencer (1961), Spencer & Kandel (1961)
$\Theta_{max}/\Theta_{min}$	—	5	Anderson *et al.* (1964), Kandel & Spencer (1961)
f_0	—	$16 \times m \simeq 9.92$	
Γ	—	$\simeq 0.24$	
β	—	$4.5 \times 10^{-3} \, R$	

• m is the concentration of GABA released per action potential in the basket cells, and is difficult to estimate. Traub & Miles (1991, p. 55) estimate that one quantum of GABA activates about 20 receptors. $n = 3$ is estimated to be the number of molecules required to activate one receptor. These figures were used to employ a statistical algorithm to find the number M_1 of GABA molecules contained in one quantum: assume that an effective number $R_{eff} < R$ of receptors can be reached by the GABA molecules contained in the quantum. The molecules are distributed randomly among these receptors but no receptor must receive more than $n = 3$ molecules. Then M_1 is the number of GABA molecules which yields, on average, 20 active receptors. With $R_{eff} = 50$, a numerical calculation yields $M_1 \approx 94$. Traub & Miles (1991) further estimate that a single inhibitory action potential releases of the order of 12 quanta of GABA. Under the assumption that each receptor receives molecules only from a single quantum, a single action potential releases about $12 M_1 \approx 1128$ molecules of GABA.

Assume that these 1128 GABA molecules are released into an effective synaptic volume of $\mathscr{V}$ measured in μ^3, so we have a concentration of $1128/\mathscr{V}$ molecules $\times \mu^{-3}$. We wish to express this in terms of moles. Keeping the numerical value of $\mathscr{V}$ but reexpressing the units in molar concentration we arrive at

$$m = \frac{1128}{\mathscr{V}} \frac{\text{molecules}}{\mu^3}$$

$$= \frac{1.128 \times 10^{18}}{\mathscr{V}} \frac{\text{molecules}}{1} \approx \frac{1.87}{\mathscr{V}} \mu M.$$

However, this is for one action potential, and if we assume that an action potential has a duration of 1 ms then this translates to an m value of

$$m = \frac{1.87 \times 10^{-3}}{\mathscr{V}} \mu M \, s.$$

From the data of Nusser (1999), inhibitory synapses have an effective cross-sectional area of $0.1–0.2 \, \mu^2$ and the synaptic gap is about $20 \times 10^{-3} \, \mu$ (Prof. C. Stevens, pers. comm.) to give an effective synaptic volume of $\mathscr{V} \simeq 2–4 \times 10^{-3} \, \mu^3$. Taking the midpoint of this range leads to $m \simeq 0.62 \, \mu M$.

Although there are a number of uncertainties in the estimation of m, our numerical investigations suggest that the system dynamics—including the firing frequencies corresponding to the

different attractors described below—do not alter significantly as m is varied.

- n is the effective number of GABA molecules required to bind to the GABA receptor for activation. This was determined to be between 2 and 3 in Nowak *et al.* (1982) and between 3 and 4 in Werman (1979). We have taken an intermediate value with $n = 3$.
- α is the ratio between the firing frequency of the inhibitory interneurons (the basket cells) and the pyramidal cells. This can be interpreted as the reciprocal of the number of pyramidal cell action potentials required to elicit one basket cell action potential. Based on the data presented in (Traub & Miles, 1991, p. 65, Table 3.2 and Fig. 3.8) $\alpha \simeq 0.3 - 0.4$ and we have taken $\alpha = 0.4$.
- κ is the slope of the firing frequency vs. membrane potential relation. From the data of Kandel & Spencer (1961, Fig. 8A) this relationship is linear as we assumed in eqn (17), and $\kappa = 26 \times 10^{10}$ (amp-s)$^{-1}$. With a membrane resistance of $R_m = 13 \times 10^6 \, \Omega$ (Kandel & Spencer 1961; Spencer & Kandel, 1961) this translates to $\kappa = 20$ (mV s)$^{-1}$.
- τ_{min} is the minimal value of the delay that is expected from the most rapidly conducting (largest) fibres in the recurrent pathway. From the data of Anderson *et al.* (1964, Fig. 3A and p. 596) the minimal latency for the inhibition with commissural stimulation of 5 times threshold was $\tau_{min} = 5.6$ ms.
- τ_{max} was determined from the same source as τ_{min} (Anderson *et al.*, 1964) where a latency of 9.1 ms was observed with a commissural stimulation of 1.02 times threshold.
- Θ_{min} is the minimum threshold for firing. From Kandel & Spencer (1961, Fig. 8A) the rheobase current in one cell was $\sim 6.5 \times 10^{-10}$ A, which is at the upper end of the range of rheobase currents in Spencer and Kandel (1961, Table 2) who report a rheobase ranging from 1.0 to 5.0×10^{-10} A. With a membrane resistance of $R_m = 13 \times 10^6 \, \Omega$ (Kandel & Spencer, 1961; Spencer & Kandel, 1961) this range of rheobase currents corresponds to a threshold range with a minimum of $\Theta_{min} = 1.3$ mV. This is about half of the minimum firing levels reported in Kandel & Spencer (1961, Table 1) which range from 2.7 to 5.2 mV. We have chosen a $\Theta_{min} = 2$ mV.

- $\Theta_{max}/\Theta_{min}$ is taken to be 5 in accordance with the data of Kandel & Spencer (1961, Table 2), and the data of Anderson *et al.* (1964).

The data on Θ_{min}, Θ_{max}, τ_{min} and τ_{max} are interesting when considered within the context of the relationship $\Theta = \Theta_0 \tau^{-3/2b}$ derived in Section 2.1. From this relation between the threshold and the conduction delay we have

$$b = \frac{3}{2} \frac{\ln \tau_{max}/\tau_{min}}{\ln \Theta_{max}/\Theta_{min}}. \qquad (32)$$

Using the values tabulated above we obtain an approximate value of $b \simeq 0.45$, which is close to the value of 0.5 that would hold if the feedback pathway were non-myelinated. Given the conduction velocities of $0.5 \, \text{m s}^{-1}$ for pyramidal cells (Colling *et al.*, 1998) and $0.2 \, \text{m s}^{-1}$ for interneurons (Salin & Prince, 1996) the pathway is most certainly non-myelinated. This close correspondence gives us confidence in our parameter estimation as well as this portion of our model formulation.

4.2. NUMERICAL BEHAVIOUR

The dynamical system (27)–(29) was numerically investigated using a rectangular distribution of delays (A.30). [We did this in the absence of any experimental information about the way in which the delays are distributed between τ_{min} and τ_{max}. Other numerical studies using the density of the gamma distribution (results not shown) have yielded results virtually identical to those we show here, and it would appear that the primary important factors are the values of τ_{min} and τ_{max} as the results of Bernard *et al.* (2001) indicate should be the case]. Parameters were chosen from Table 1 except for the average number of GABA receptors per pyramidal cell, R, which was used as a bifurcation parameter along with the constant excitatory input e. The reason for choosing R and e is that they may be variable in the biological feedback loop under consideration:

- First, in *in vitro* experimental conditions, the experimentalist has control over the stimulation e used in studying the preparation. Second, *in vivo* the excitatory input e is likely to vary due

to the overall activity of the hippocampal network and its afferents.

• With respect to the average number of GABA receptors per cell (R) this is easily modified in the *in vitro* situation through titration with penicillin which is a GABA receptor agonist. Furthermore, a modification of the number of receptors in the post-synaptic membrane is a likely candidate for LTP and LTD (e.g. Carroll *et al.*, 1999; Shi *et al.*, 1999) and may thus vary on the longer time scale of synaptic modification.

In the following, we display the time course of the dimensionless membrane potential as a function of the dimensionless time variable, $v(\bar{t})$, and the average firing frequency of the excitatory population in its *unscaled* form, $F(t)$, for different values of the parameters R and e. $F(t)$ can be calculated from the output frequency of a single fibre with delay τ, eqn (17), and subsequent averaging over the rectangular distribution of delays (A.30). It is obtained from the dimensionless firing frequency (29) of the inhibitory population as

$$F(\tilde{f}) = \frac{\sqrt[3]{K}}{\alpha m}\tilde{f} = 20.16\tilde{f} \qquad (33)$$

and has the dimensions of Hz. As initial conditions for the dynamical system (27)–(29), we restrict ourselves to constant functions

$$v_0(\bar{t}) \equiv v_0, \quad -T_{max} < \bar{t} \leqslant 0. \qquad (34)$$

The simulations we have performed with more complicated initial functions, e.g. functions which span the unstable fixed point v_*^2, have not yielded different results (data not shown). Simulations were performed in Matlab and with xpp4w95. Some of the results were also checked using a Fortran version. Copies of the code are available from the authors.

The stability considerations of Appendix A.2 were numerically confirmed. In particular, the steady-state v_*^2 was always unstable, and v_*^3 was always stable. The dynamical properties of v_*^1, however, changed as a function of both R and e as expected from our linear analysis.

Figures 3 and 4 show the dynamics of the system for the parameter values of Table 1; in particular, $R = 1700$. In this parameter regime,
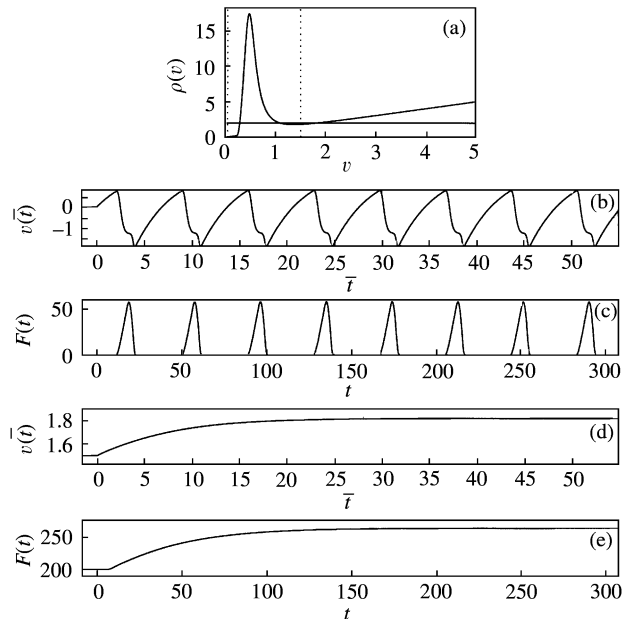

FIG. 3. System behaviour for $R = 1700$ and small input e. (a) $\rho(v)$ which is non-monotone and gives rise to three steady states v_*^1, v_*^2, v_*^3. (—) horizontal line: $e = 2$. ($\cdots$) vertical lines: two initial conditions $v_0 = 0.05$ and 1.5. For $v_0 = 0.05$, the post-synaptic cell activity approaches a stable limit cycle while it converges to the steady-state v_*^3 for $v_0 = 1.5$. (b,c) Rescaled membrane potential $v(\bar{t})$ and unscaled firing frequency $F(t)$ for $v_0 = 0.05$. (d,e) $v(\bar{t})$ and $F(t)$ for $v_0 = 1.5$. Remember that the time $\bar{t}$ is dimensionless and the time t is measured in ms. Remaining parameters were chosen from Table 1.

$\rho(v)$ is non-monotone, and there may be one, two, or three steady states depending on the value of the excitatory input e. The steady-state v_*^1 is unstable. In addition, the dynamics of the system in the neighbourhood of v_*^1 depend on the size of the input, e. For small input, i. e. in the regime of a single steady-state v_*^1 and for small input in the regime of three steady states, a stable limit cycle appears in the neighbourhood of v_*^1. Trajectories are either attracted to this limit cycle or to the steady-state v_*^3 (cf. Fig. 3). The periodic oscillation of the membrane potential in the neighbourhood of v_*^1 may result in one or two spikes per oscillation period, i. e. the period of this oscillation rather than $F(t)$ might appear in an empirical study of the hippocampal feedback loop. The eventual maximal firing frequency in Fig. 3(c) is about 58 Hz, while the frequency of the oscillation is about 26 Hz. It is only weakly dependent on R (data not shown).
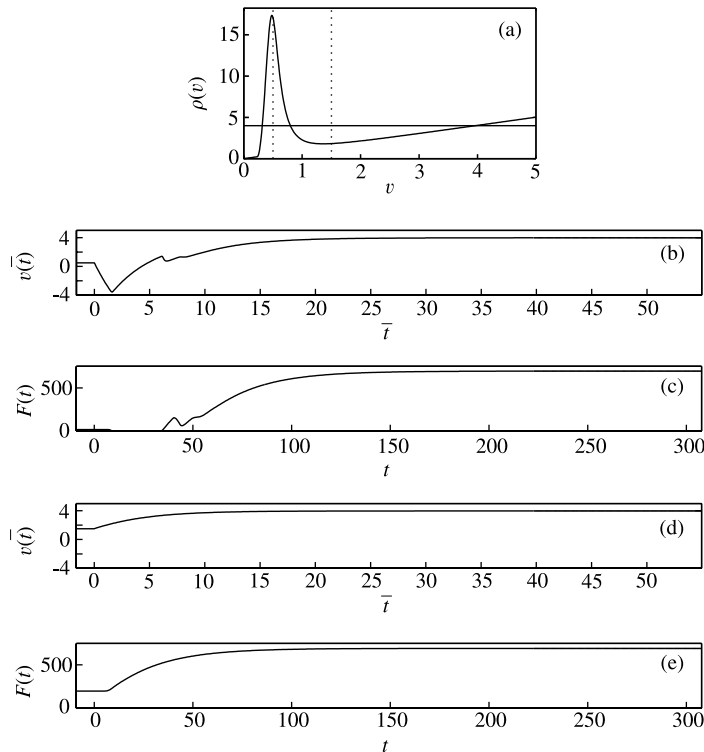
FIG. 4. System behaviour for $R = 1700$ and large input e. (a) $\rho(v)$ which is the same as in Fig. 3. (——) horizontal line: $e = 4$. ($\cdot \cdot \cdot \cdot$) vertical lines: two initial conditions $v_0 = 0.5$ and 1.5. For both values v_0, the post-synaptic cell approaches the steady-state v_*^3. (b,c) Rescaled membrane potential $v(\bar{t})$ and unscaled firing frequency $F(t)$ for $v_0 = 0.5$. (d,e) $v(\bar{t})$ and $F(t)$ for $v_0 = 1.5$. The time $\bar{t}$ is dimensionless and the time t is measured in ms. Remaining parameters were chosen from Table 1.

The firing frequency $F(t)$ corresponding to the steady-state v_*^3 is about 264 Hz [Fig. 3(e)].

For higher inputs e in the regime of three steady states, the stable oscillation vanishes, and v_*^3 is globally stable and numerically attracts solutions with all initial conditions (Fig. 4). The firing frequency corresponding to v_*^3 is about 695 Hz.

As R is decreased, v_*^1 becomes asymptotically stable. Figure 5 shows the system for $R = 50$ where $\rho(v)$ is still non-monotone. In this case, $e = 0.9$ and there are three steady-states. The system is bistable and may switch between the stable steady states v_*^1 and v_*^3 by varying the external input. Two sample solutions are shown in Fig. 5 yielding firing frequencies of about 12 and 65 Hz for v_*^1 and v_*^3, respectively.

In most bistable cases we encountered, the unstable steady-state v_*^2 is a basin boundary for v_*^1 and v_*^3 if constant initial functions (34) are employed. In rare cases (e. g. for $R = 100$, $e = 1.9$, $v_0 = 0.3$; data not shown), however, initial conditions to the left of v_*^1 will result in the trajectory converging to v_*^3. This behaviour is due to the delay in the system and the attendant infinite-dimensional phase space.

For very small values of R, inequality (A.14) for the function $\rho(v)$ to be monotone increasing is satisfied, and a single steady-state v_*^1 exists. In all cases with monotone $\rho(v)$, v_*^1 was found to be globally asymptotically stable resulting in a regular post-synaptic neural firing. An example is given in Fig. 6, where $R = 10$, $e = 0.9$, and the firing frequency in the steady state is about 80 Hz.

5. Discussion

The model that has been developed and analysed here is an extension of Mackey and an der Heiden (1984). The primary extension of the current model is the inclusion of the distribution of delay times and the fact that this distribution is state dependent. A variety of
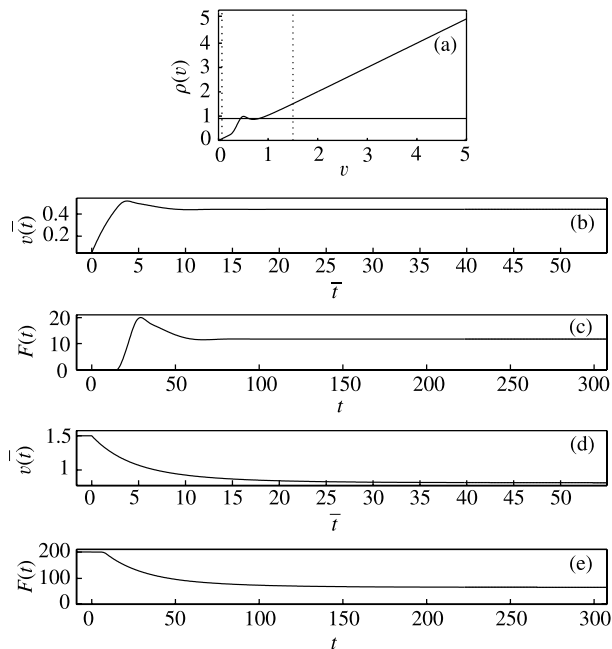
FIG. 5. System behaviuor for $R = 50$. (a) $\rho(v)$ is not monotone; there are three steady states v_*^1, v_*^2, v_*^3 in the post-synaptic population. (—) horizontal line: excitatory input $e = 0.9$. ($\cdot \cdot \cdot \cdot$) vertical lines: two initial conditions $v_0 = 0.05$ and 1.5. (b, c) Rescaled membrane potential $v(\bar{t})$ and unscaled firing frequency $F(t)$ for $v_0 = 0.05$; the trajectories approach the steady-state v_*^1. (d,e) $v(\bar{t})$ and $F(t)$ for $v_0 = 1.5$; the trajectories approach the steady-state v_*^3. The time $\bar{t}$ is dimensionless and t is measured in ms. Remaining parameters were chosen from Table 1.

numerical simulations (that we have not shown in this paper, but which will be presented elsewhere) illustrate that with the original parameters of Mackey & an der Heiden (1984) and a state-dependent distribution of delays, a progressive increase in the variance of the distribution leads to a loss of the higher-order bifurcations and chaotic behaviour found in Mackey & an der Heiden (1984). On the other hand, with the current estimates of the parameters and maintaining the rectangular distribution of delays we have also seen a broad spectrum of dynamic behaviours by simply increasing the parameter Γ from the value of 0.24. Thus it is clear that the presence of the state-dependent distribution of delays does not destroy the higher-order bifurcation pattern leading to chaos in this case, but rather shifts it to a different region of parameter space and a region that is apparently physiologically inappropriate for the recurrent inhibitory system we have used as an example.
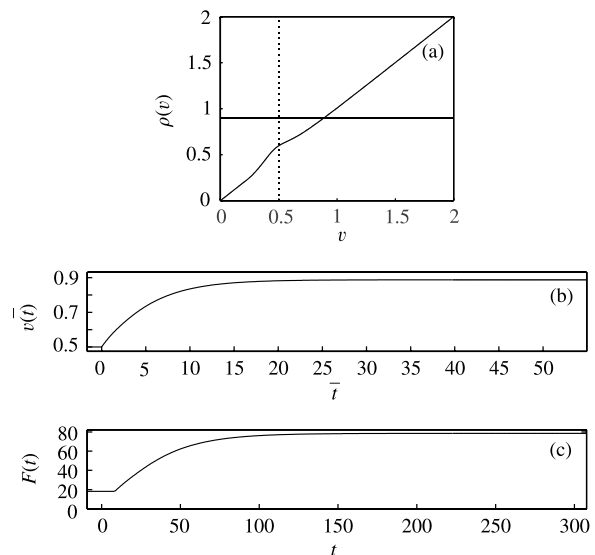

FIG. 6. System behaviour for $R = 10$. (a) $\rho(v)$ is monotone increasing; there is a single globally stable steady-state v_*^1 in the post-synaptic population. (—) horizontal line: excitatory input $e = 0.9$. ($\cdot \cdot \cdot \cdot$) vertical line: initial condition $v_0 = 0.5$. (b) Rescaled membrane potential $v(\bar{t})$. (c) Unscaled firing frequency $F(t)$ of the excitatory population. The time $\bar{t}$ is dimensionless and t is measured in ms. All other parameters were chosen from Table 1.

One aspect of the qualitative dynamics observed in Mackey & an der Heiden (1984) and which is still found here is the bistability in solution behaviour. The bistability comprising two fixed points corresponds to switching between behaviours with firing frequencies 10–25 Hz on the one hand with a second region with frequencies of 30–100 Hz (Fig. 5). The possible relation of this bistability to any physiologically observed bistability is unclear, but we do note that it corresponds to the observed shift between the γ to β frequencies found in hippocampal slice preparations and which have been described in Traub *et al.* (1999).

In our model, the state of the whole post-synaptic cell population is represented by the membrane potential $v(\bar{t})$ of an average neuron. To check if this is a valid simplification, a network model consisting of 500 individual graded response cells was designed, each with its own membrane potential dynamics described by the equations (27) and (28). The output firing rate of a neuron is chosen to be the positive part of its potential minus a threshold value. As thresholds and signal conduction velocities

covary as described in Section 2.1, the thresholds of individual cells are set according to the rectangular delay distribution between a minimal value θ_{min} and a maximal value θ_{max}. Each neuron is inhibited by the delayed output of all cells in the network, including itself. This results in a cumulative inhibition caused by the previous firing rates corresponding to eqn (29). Note that the feedback input is the same for all cells, and as a consequence, their potentials all approach the same fixed point or limit cycle during simulation. This is especially the case if the neurons are started with randomly chosen v_0, or if half of the cells is initialized with v_0 near one of the fixed points, the other half near the other. Although several starting conditions and parameter regimes were tested, a split into two or more subpopulations with different time-dependent potentials could not be observed. Thus, the population model dynamics seem to mimic those observed in the simplified model we have presented and analysed in this paper. We will present a full and detailed account of these population model dynamics in a future communication.

REFERENCES

AN DER HEIDEN, U. (1979). *Analysis of Neural Networks.* New York: Springer-Verlag.

AN DER HEIDEN, U. (1991). Neural networks: flexible modelling, mathematical analysis, and applications. In: Paseman, F. & Doebner, H. D., (Eds.), *Neurodynamics*:

Proceedings of the Ninth Summer Workshop on Mathematical Physics (pp. 49–95). Singapore: World Scientific.

AN DER HEIDEN, U. & Mackey, M. C. (1982). The dynamics of production and destruction: Analytic insight into complex behaviour. *J. Math. Biol.* **16,** 75–101

AN DER HEIDEN, U. & Mackey, M. C. (1987). Mixed feedback: a paradigm for regular and irregular oscillations. In: Rensing, L., an der Heiden, U., Mackey, M. C. (Eds.), *Temporal Disorder in Human Oscillatory Systems* (pp. 30–36). New York, Berlin & Heidelberg, Springer-Verlag.

AN DER HEIDEN, U., Mackey, M. C. & WALTHER, H. O. (1981). Complex oscillations in a simple deterministic neuronal network. *Lectures Appl. Math.* **19,** 355–360.

ANDERSON, P., ECCLES, J. C. & LØYNING, Y. (1964). Location of postsynaptic inhibitory synapses on hippocampal pyramids. *J. Neurophysiol.,* **27,** 592–607.

BERNARD, J., BÉLAIR, S. & MACKEY, M. C. (2001). Sufficient conditions for stability of linear differential equations with distributed delay. *Discrete Continuous Dynam. Sys.* **1,** 233–256.

CARR, C. E. & KONISHI, M. (1990). A circuit for detection of interaural time differences in the brain stem of the barn owl. *J. Neurosci.* **10,** 3227–3246.

CARROLL, R. C., LISSIN, D. V., VON ZASTROW, M., NICOLL, R. A. & MALENKA, R. C. (1999). Rapid redistribution of glutamate receptors contributes to long-term depression in hippocampal cultures. *Nature Neurosci.* **2,** 454–460.

CASTELFRANCO, A. M. & STECH, H. W. (1987). Periodic solutions in a model of recurrent neural feedback. *SIAM J. Appl. Math.* **47,** 573–588.

COLLING S. B., STANFORD, I. M., TRAUB, R. D. & JEFFREYS, J. G. R. (1998). Limbic gamma rhythms: I. Phase locked oscillations in hippocampal CA1 and subiculum. *J. Neurophysiol.* **80,** 155–161.

DIEZ MARTINEZ, O. & SEGUNDO, J. P. (1983). Behavior of a single neuron in a recurrent inhibitory loop. *Biol. Cybern.* **47,** 33–41.

ERMENTROUT, G. B. & KOPELL, N. (1998). Fine structure of neural spiking and synchronization in the presence of conduction delays. *Proc. Natl Acad. Sci. U.S.A.* **95,** 1259–1264.

ERNST U., PAWELZIK, K. & GEISEL, T. (1995). Synchronization induced by temporal delays in pulse-coupled oscillators. *Phys. Rev. Lett.* **74,** 1570–1573.

EURICH, C. W., PAWELZIK, K., ERNST, U., COWAN, J. D. & MILTON, J. G. (1999). Dynamics of self-organized delay adaptation. *Phys. Rev. Lett.* **82,** 1594–1597.

EURICH, C. W., PAWELZIK, K., ERNST, U., THIEL, A., COWAN, J. D. & MILTON, J. G. (2000). Delay adaptation in the nervous system. *Neurocomputing* **32–33,** 741–748.

GUEVARA, M. R., GLASS, L., MACKEY, M. C. & SHRIER, A. (1983). Chaos in neurobiology. *IEEE Trans. Systems, Man Cybern.* **13,** 790–798.

JACK, J. J. B., NOBLE, D. & TSIEN, R. W. (1975). *Electric Current Flow in Excitable Cells.* Oxford: Clarendon Press.

KANDEL, E. R. & SPENCER, W. A. (1961). Electrophysiology of hippocampal neurons. II. After potentials and repetitive firing. *J. Neurophysiol.* **24,** 243–259.

MACKEY, M. C. & AN DER HEIDEN, U. (1984). The dynamics of recurrent inhibition. *J. Math. Biol.,* **19,** 211–225.

MEGÍAS, M., EMRI, Z. S., FREUND, T. F. & GULYÁS, A. I., (2001). Total number and distribution of inhibitory and excitatory synapses on hippocampal CA1 pyramidal cells. *Neuroscience* **102,** 527–540.

MILTON, J. (1996). *Dynamics of Small Neural Networks.* American Mathematical Society, Providence, R.I.

MILTON, J. G., AN DER HEIDEN, U., LONGTIN, A. & MACKEY, M. C. (1990). Complex dynamics and noise in simple neural networks with delayed mixed feedback. *Biomed. Biochim. Acta.* **49,** 697–707.

MILTON, J. G., LONGTIN, A., BEUTER, A., MACKEY, M. C. & GLASS, L. (1989). Complex dynamics and bifurcations in neurology. *J. Theor. Biol.* **138,** 129–147.

NOWAK, L. M., YOUNG, A. B. & MACDONALD, R. L., (1982). GABA and bicuculline actions on mouse spinal cord and cortical neurons in cell culture. *Brain Res.* **244,** 155–164.

NUSSER, Z. (1999). A new approach to estimate the number, density and variability of receptors at central synapses. *Europ. J. Neurosci.* **11,** 745–752.

PLANT, R. E. (1981). A Fitzhugh differential-difference equation modeling recurrent neural feedback. *SIAM J. Appl. Math.* **40,** 150–162.

SALIN, P. A. & PRINCE, D. (1996). A. Electrophysiological mapping of GABA$_A$ receptor mediated inhibition in adult rat somatosensory cortex. *J. Neurophysiol.* **75,** 1589–1600.

SHI, S.-H., HAYASHI, Y., PETRALIA, R. S., ZAMAN, S. H., WENTHOLD, R. J., SVOBODA, K. & MALINOW, R. (1999). Rapid spine delivery and redistribution of AMPA receptors after synaptic NMDA receptor activation. *Science* **284,** 1811–1816.

SPENCER, W. A. & KANDEL, E. R. (1961). Electrophysiology of hippocampal neurons. III. Firing level and time constant. *J. Neurophysiol.* **24,** 260–271.

STANFORD, L. R. (1987). Conduction velocity variations minimize conduction time differences among retinal ganglion cell axons. *Science* **238,** 358–360.

TRAUB, R. D. & BIBBIG, A. (2000). A model of high frequency ripples in the hippocampus based on synaptic coupling plus axon–axon gap junctions between pyramidal neurons. *J. Neurosci.* **20,** 2086–2093.

TRAUB, R. D. & MILES, R. (1991). *Neuronal Networks of the Hippocampus.* Cambridge University. Press, New York.

TRAUB, R. D., JEFFREYS, J. G. R., MILES, R., WHITTINGTON, M. A. & TÓTH, K. (1994). A branching dendritic model of a rodent CA3 pyramidal neurone. *J. Physiol.* **481,** 79–95.

TRAUB, R. D., MILES, R. & JEFFREYS, J. G. R. (1993). Synaptic and intrinsic conductances shape picrotoxin induced synchronized after discharges in the guinea pig hippocampal slice. *J. Physiol.* **461,** 525–547.

TRAUB, R. D., SCHMITZ, D., JEFFREYS, J. G. R. & DRAGUHN, A. (1999a). High frequency population oscillations are predicted to occur in hippocampal pyramidal neuronal networks interconnected by axoaxonal gap junctions. *Neuroscience* **92,** 407–426.

TRAUB, R. D., WHITTINGTON, M. A., BUHL, E. H., JEFFREYS, J. G. R. & FAULKNER, H. J. (1999b). On the mechanism of the $\gamma \to \beta$ frequency shift in neuronal oscillations induced in rat hippocampal slices by tetanic stimulation. *J. Neurosci.* **19,** 1088–1105.

TRAUB, R. D., WHITTINGTON, M. A., COLLING, S. B., BUZSÁKI, G. & JEFFREYS, J. G. R. (1996). Analysis of gamma rhythms in the rat hippocampus *in vitro* and *in vivo*. *J. Physiol.* **493,** 471–484.

TRAUB, R. D., WONG, R. K. S., MILES, R. & MICHELSON, H. (1991). A model of a CA3 hippocampal pyramidal neuron incorporating voltage-clamp data on intrinsic conductances. *J. Neurophysiol.* **66,** 635–650.

TUCKWELL, H. C. (1978). Recurrent inhibition and after-hyperpolarization: effects on neuronal discharge. *Biol. Cybern.* **30,** 115–123.

WERMAN, R. (1979). Stoichiometry of GABA-receptor interactions: GABA modulates the glycine–receptor interaction allosterically in a vertebrate neuron. *Adv. Exp. Med. Biol.* **123,** 287–301.

WILSON, H. R. & COWAN, J. D. (1972). Excitatory and inhibitory interactions in localized populations of model neurons. *Biophys. J.* **12,** 1–23.

WILSON, H. R. & COWAN, J. D. (1973). A mathematical theory of the functional dynamics of cortical and thalamic nervous tissue. *Kybernetik* **13,** 55–80.

Appendix A

Model Analysis

In this appendix, we give the full analysis of the model as formulated in eqns (19) and (20). We start in Appendix A.1 with an examination of the steady states of the model. Their local stability is the subject of Appendix A.2.

A.1. STEADY STATES

The dimensionless system defined by eqns (27)–(29) can have one, two or three steady states. To see how this can come about, consider the following.

For $v(\bar{t}) \equiv v = $ constant, $\tilde{f}$ takes the form

$$\tilde{f}(v) \equiv \mathscr{F}(v) = f_0 \int_{T(v)}^{T_{max}} [v - \theta(T)]\bar{\xi}(T)\, dT, \quad \text{(A.1)}$$

with

$$T(v) = \frac{\tau(v)}{\tau_{min}} = v^{-2b/3} \geqslant 1 \qquad \text{(A.2)}$$

and

$$T_{max} = \frac{\tau_{max}}{\tau_{min}}. \qquad \text{(A.3)}$$

$\mathscr{F}(v)$ has the following properties:

(i) If $v < \theta_{min} = \Theta_{min}/\Theta_{max} < 1$ then there will be no excitation of the excitatory population of cells so $\mathscr{F} \equiv 0$.

(ii) If $v \in [\theta_{min}, 1]$, then the lower bound on the integral in eqn (A.1) is a monotone decreasing function of v so we know that in this region $\mathscr{F}$ is a monotone increasing function of v.

(iii) If $v > \theta_{max} \equiv 1$ then

$$\mathscr{F}(v) = f_0 \int_{T_{min}=1}^{T_{max}} [v - \theta(T)]\bar{\xi}(T)\,\mathrm{d}T$$

$$= f_0 v - f_0 \int_1^{T_{max}} \theta(T)\bar{\xi}(T)\,\mathrm{d}T, \qquad (A.4)$$

so for $v > \theta_{max} = 1$ we know that $\mathscr{F}$ is a linearly increasing function of v.

Thus, to summarize $\mathscr{F} = 0$ at $v = e = \theta_{min}$ and for $v > \theta_{min}$ we know that $\mathscr{F}$ is a monotone increasing function of v.

The steady state(s) of this system are denoted by v_* and are defined from the condition that $\mathrm{d}v/\mathrm{d}\bar{t} \equiv 0$. Equations (27), (28) and (A.1) yield the steady-state condition

$$e - v_* = \mathscr{H}(v_*), \qquad (A.5)$$

where

$$\mathscr{H}(v) = \frac{\beta}{\Gamma}\mathscr{G}(\mathscr{F}(v)). \qquad (A.6)$$

We rewrite eqn (A.1) in the form

$$\mathscr{F}(v) = f_0 v \mathscr{I}_1(v) - f_0 \mathscr{I}_2(v), \qquad (A.7)$$

wherein

$$\mathscr{I}_1(v) = \int_{T(v)}^{T_{max}} \bar{\xi}(T)\,\mathrm{d}T \quad \text{and}$$

$$\mathscr{I}_2(v) = \int_{T(v)}^{T_{max}} \theta(T)\bar{\xi}(T)\,\mathrm{d}T. \qquad (A.8)$$

The derivative of $\mathscr{H}(v)$ is then given by

$$\mathscr{H}'(v) = \frac{\beta}{\Gamma} f_0 \mathscr{I}_1(v)\mathscr{G}'(\mathscr{F}(v)). \qquad (A.9)$$

To study the number of possible steady states, we will use a graphical approach since it is the most transparent. Using the information about the behaviour of $\mathscr{F}(v)$ as described above, eqn (A.5) can be evaluated graphically as shown in Fig. 7 for $n > 1$. The left-hand side of eqn (A.5) is a linearly decreasing function of v and thus (for all other parameters being fixed) depending on the value of the parameters Γ, e or β we may have one [Fig. 7(a), (b) and (f)], two [Fig. 7(c) and (e)], or three [Fig. 7(d)] intersections with a corresponding number of steady states which we label from left to right as v_*^i, $i = 1, 2, 3$ with $0 \leqslant v_*^1 \leqslant v_*^2 \leqslant v_*^3$. In the case of Fig. 7(a), the steady-state $v_*^1 \leqslant \theta_{min}$ consists of no firing and $\mathscr{F}(v_*) = 0$.

Introducing a function

$$\rho(v) \equiv v + \mathscr{H}(v), \qquad (A.10)$$

the steady-state eqn (A.5) can be written as

$$e = \rho(v_*). \qquad (A.11)$$

If ρ is a monotone increasing function of v, a unique steady-state v_* is given by eqn (A.11). According to eqn (A.9)

$$\rho'(v) = 1 + \mathscr{H}'(v) = 1 + \frac{\beta f_0 \mathscr{I}_1(v)}{\Gamma}\mathscr{G}'(\mathscr{F}(v)). \qquad (A.12)$$

A necessary and sufficient condition for ρ to be monotone increasing is that the inequality

$$\mathscr{H}'(v) \geqslant -1, \qquad (A.13)$$

or equivalently

$$\mathscr{G}'(\mathscr{F}(v)) \geqslant -\frac{\Gamma}{\beta f_0 \mathscr{I}_1(v)} \qquad (A.14)$$

must hold *for all* v. Note that condition (A.14) includes the case $v \leqslant \theta_{min} = T_{max}^{-3/2b}$ where $\mathscr{I}_1(v) \equiv 0$. Consequently, this is a sufficient condition for a unique steady-state v_*. An example where inequality (A.14) is satisfied is shown in Figs 8(a) and 9. Fig. 8(a) shows the graph of the monotone function $\rho(v)$. Figure 9 illustrates inequality (A.14), and shows that increasing the parameter β may lead to the violation of inequality (A.14).

If inequality (A.14) does not hold for all v then ρ has two local extrema v_1 and v_2 ($v_1 < v_2$) as
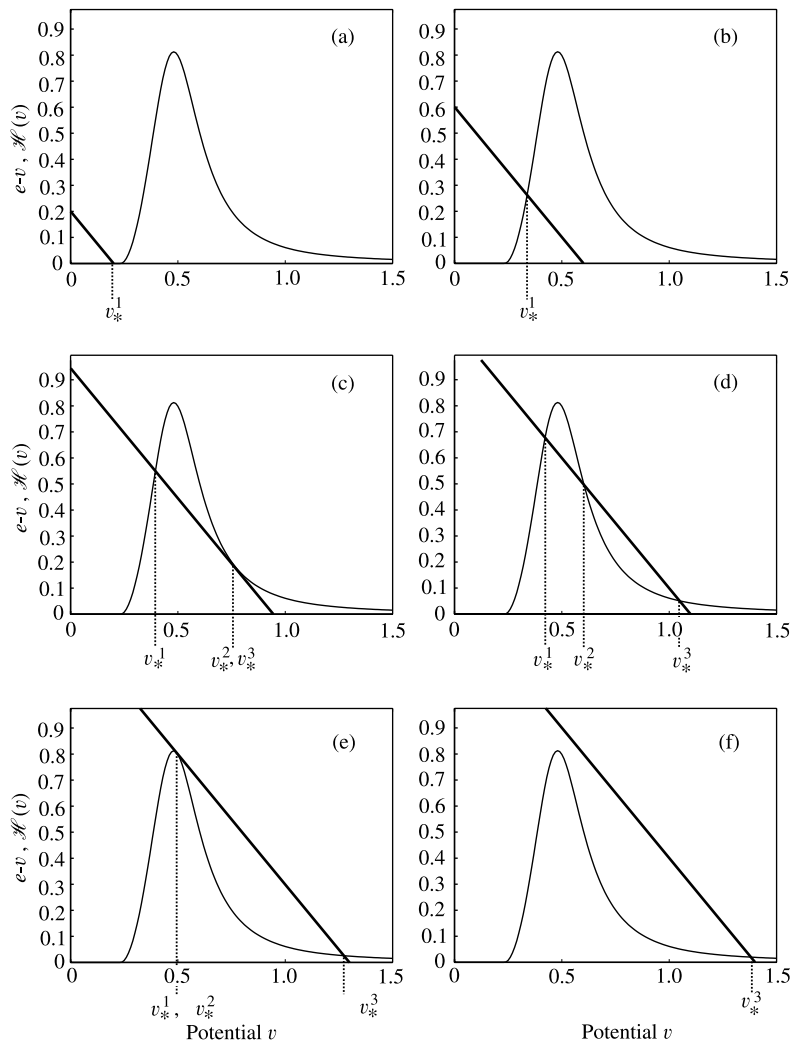
FIG. 7. A plot (for $n > 1$) of the left- and right-hand sides of eqn (A.5) as a function of the membrane potential v. As any one of the parameters Γ, e, or R is varied with all other parameters held fixed, we may have one [(a), (b) and (f)], two [(c) and (e)] or three [(d)] steady states. Here, both functions $e - v$ and $\mathscr{H}(v)$ were determined assuming a delay distribution with a rectangular density given by eqn (A.30) and the parameters from Table 1 except for $\Gamma = 5$ which was chosen for better visibility of the different cases. In (a) $e = 0.2$, (b) $e = 0.6$, (c) $e \approx 0.95$, (d) $e = 1.1$, (e) $e \approx 1.3$, and (f) $e = 1.4$.

shown in Fig. 8(b). By defining $e_1 = \rho(v_1)$ and $e_2 = \rho(v_2)$ we may distinguish the three cases

(i) For $e_2 < e < e_1$ there are three steady states.

(ii) For $e = e_1$ and $e = e_2$ there are two steady states.

(iii) For $e < e_2$ and $e > e_1$ there is a unique steady state.

A.2. STABILITY OF STEADY STATES

We now turn to a consideration of the stability of the steady states, defined implicitly by eqns

(A.5) and (A.1), and how that stability may be lost. In general, the question that one would always like to be able to examine is the global stability of a steady state to all perturbations. However, there are no general global stability results for systems with dynamics described by eqns (27)–(29), and consequently the usual approach is to examine the stability of v_* in the face of very small deviations away from the steady state. This type of examination is called an analysis of the *local* stability of v_*.

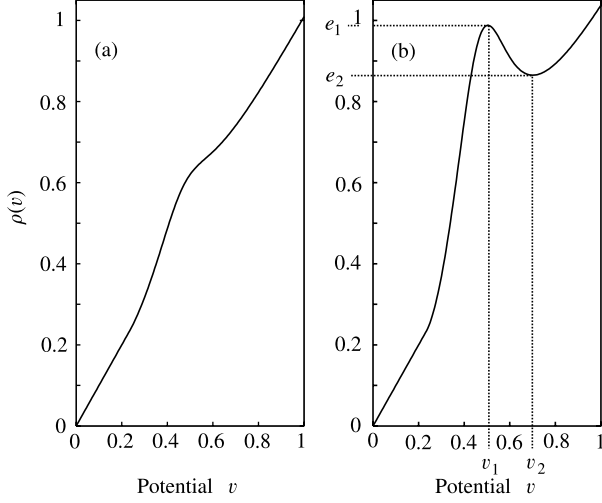Before we proceed to the steady states of the full system we briefly consider the case of a fixed

FIG. 8. The graph of $\rho(v)$ when: (a) condition (A.14) holds and there is a single steady-state solution v_* of (A.5); (b) inequality (A.14) does not hold and there may be one, two, or three steady states. The function $\rho(v)$ was determined assuming a delay distribution with a rectangular density given by eqn (A.30) and standard parameters from Table 1 except for (a) $R = 15$, (b) $R = 50$.
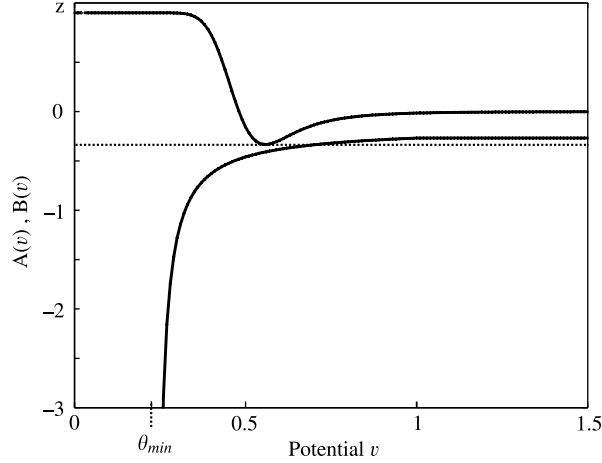

FIG. 9. A plot of eqn (A.14) when the condition is satisfied and there is a single steady-state solution v_* of (A.5). Both functions, $A(v) \equiv \mathscr{G}'(\mathscr{F}(v))$ (top) and $B(v) \equiv -\Gamma/\beta f_0 \mathscr{I}_1(v)$ (bottom), were obtained from the rectangular delay distribution (A.30) and standard parameters from Table 1 except for $R = 20$.

point $v_* < \theta_{min}$ as shown in Fig. 7(a). For v in a neighbourhood of v_*, $\mathscr{F}(v) \equiv 0$ as was argued in condition (i) after eqn. (A.3). In this situation there is no excitation of the excitatory population and consequently no inhibitory feedback, $i \equiv 0$. The steady-state condition (A.5)

reduces to

$$v_* = e \qquad (A.15)$$

which holds for $e < \theta_{min}$. Equation (27) becomes a linear ordinary differential equation,

$$\frac{dv}{d\bar{t}} = \Gamma(e - v), \qquad (A.16)$$

whose solution is given by

$$v(\bar{t}) = v_0 e^{-\Gamma \bar{t}} + e(1 - e^{-\Gamma \bar{t}}), \qquad (A.17)$$

where $v_0 \equiv v(\bar{t} = 0) < \theta_{min}$. The steady state $v_* = e$ is locally stable.

To examine the local stability for $e \geqslant \theta_{min}$ (corresponding to Fig. 7(b)–(f) we write out eqns (27)–(29) for small deviations z of v from v_*, so $v(\bar{t}) = v_* + z(\bar{t})$. In the linear approximation this gives

$$\frac{dz}{dt} \simeq -\Gamma_z - \beta f_0 \mathscr{G}'(\mathscr{F}(v_*)) \int_{T(v_*)}^{T_{max}} z_T \bar{\xi}(T) \, dT. \quad (A.18)$$

To proceed, we make the *ansatz* that the deviation z from the steady state has the form $z(\bar{t}) \simeq \exp(\lambda \bar{t})$, substitute this into eqn (A.18), carry out the indicated integrations, and finally obtain

$$\lambda + \Gamma = -\beta f_0 \mathscr{G}'(\mathscr{F}(v_*)) \int_{T(v_*)}^{T_{max}} e^{-\lambda T} \bar{\xi}(T) \, dT$$

$$= -\beta f_0 \mathscr{G}'(\mathscr{F}(v_*)) \mathscr{J}(\lambda, v_*), \qquad (A.19)$$

where

$$\mathscr{J}(\lambda, v) \equiv \int_{T(v)}^{T_{max}} e^{-\lambda T} \bar{\xi}(T) \, dT. \qquad (A.20)$$

Note that $\mathscr{I}_1(v) = \mathscr{J}(0, v)$, and therefore $\mathscr{H}'(v)$ can be written as

$$\mathscr{H}'(v) = \frac{\beta}{\Gamma} f_0 \mathscr{G}'(\mathscr{F}(v)) \mathscr{J}(0, v). \qquad (A.21)$$

Assume that the eigenvalue solutions of (A.19) are complex conjugate $\lambda = \mu + i\omega$ so the eigenvalue eqn (A.19) takes the form

$$\mu + i\omega + \Gamma = -\beta f_0 \mathscr{G}'(\mathscr{F}(v_*))$$

$$\times \int_{T(v_*)}^{T_{max}} e^{-\mu T} e^{-i\omega T} \bar{\xi}(T) \, dT. \quad (A.22)$$

Separating eqn (A.22) into its real and imaginary parts we have

$$\mu + \Gamma = -\beta f_0 \mathcal{G}'(\mathcal{F}(v_*))$$
$$\times \int_{T(v_*)}^{T_{max}} e^{-\mu T} \cos(\omega T) \bar{\xi}(T) \, dT \quad \text{(A.23)}$$

and

$$\omega = \beta f_0 \mathcal{G}'(\mathcal{F}(v_*)) \int_{T(v_*)}^{T_{max}} e^{-\mu T} \sin(\omega T) \bar{\xi}(T) \, dT. \quad \text{(A.24)}$$

Using eqns (A.23) and (A.24) we now prove two propositions concerning the local stability of steady states and apply them to the different cases discussed in Appendix A.1.

Proposition 1. *If* $\mathcal{H}'(v_*) < -1$ *then the steady-state* v_* *is unstable.*

Proof. We show that there exists a real positive eigenvalue. Equation (A.24) is satisfied for $\omega = 0$. In this case, eqn (A.23) results in

$$\mu + \Gamma = -\beta f_0 \mathcal{G}'(\mathcal{F}(v_*)) \mathcal{J}(\mu, v_*). \quad \text{(A.25)}$$

For negative $\mathcal{G}'(\mathcal{F}(v_*))$ the right-hand side of eqn (A.25) is a monotone decreasing function of μ [see Fig. 10(a)] which intersects the ordinate at $\beta f_0|\mathcal{G}'(\mathcal{F}(v_*))|\mathcal{J}(0, v_*) = \Gamma|\mathcal{H}'(v_*)|$. Therefore, the graph of the linear function $\mu + \Gamma$ intersects the graph of eqn (A.25) at $\mu > 0$ if $|\mathcal{H}'(v_*)| > 1$ or $\mu < 0$ if $|\mathcal{H}'(v_*)| < 1$. Thus for $|\mathcal{H}'(v_*)| > 1$ there exists a positive μ which satisfies eqn (A.25) which is sufficient for instability of the steady state. This situation is shown in Fig. 10(a).

Proposition 2. *If* $-1 < \mathcal{H}'(v_*) < 1$ *then the steady-state* v_* *is locally asymptotically stable.*

Proof. The function

$$\beta f_0|\mathcal{G}'(\mathcal{F}(v_*))|\mathcal{J}(\mu, v_*) \equiv$$
$$\beta f_0|\mathcal{G}'(\mathcal{F}(v_*))| \int_{T(v)}^{T_{max}} e^{-\mu T} \bar{\xi}(T) \, dT \quad \text{(A.26)}$$

is an upper bound to the right-hand side of eqn (A.23) regardless of ω. Equation (A.26) is a monotone decreasing function of μ [see
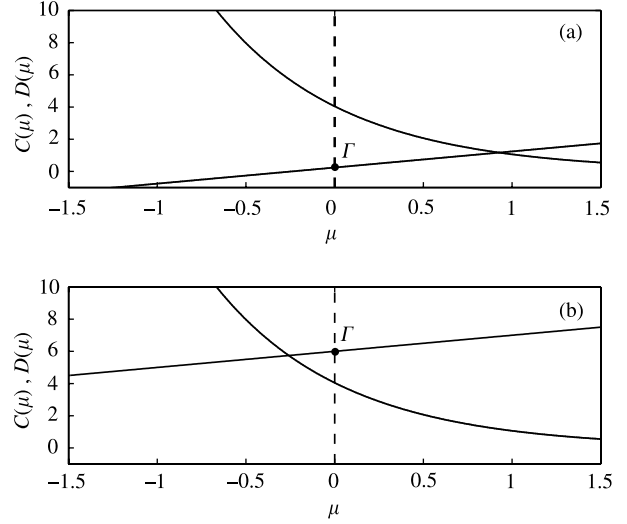

FIG. 10. Graphical representation of the stability conditions under consideration in Proposition 1 (a) and Proposition 2 (b) demonstrating that the functions $C(\mu) \equiv \beta f_0|\mathcal{G}'(\mathcal{F}(v_*))|\mathcal{J}_1(\mu, v_*)$ and $D(\mu) \equiv \mu + \Gamma$ intersect at some positive value of μ (in a) or negative value of μ (in b). In both cases, $C(\mu)$ was obtained from the rectangular delay distribution (A.30) and standard parameters from Table 1 except for (b) $\Gamma = 6$. In both cases, $v_* = 0.8$.

Fig. 10(b)] which intersects the ordinate at $\beta f_0|\mathcal{G}'(\mathcal{F}(v_*))|\mathcal{J}(0, v_*) = \Gamma|\mathcal{H}'(v_*)|$. Therefore, the graph of the linear function $\mu + \Gamma$ intersects the graph of eqn (A.26), and consequently also the right-hand side of eqn (A.23), at $\mu < 0$ if $|\mathcal{H}'(v_*)| < 1$. In this case, the real part μ of any eigenvalue is negative, and the steady-state v_* is asymptotically stable. Fig. 10(b) illustrates the argument. The results of Propositions 1 and 2 are shown in Fig. 11(a).

The stability of the steady-states v_*^1, v_*^2 and v_*^3 is determined from Propositions 1 and 2 and from the following relations that are easy to derive:

$$\mathcal{H}'(v_*^1) \geqslant -1, \quad \text{(A.27)}$$

$$\mathcal{H}'(v_*^2) \leqslant -1 \quad \text{(A.28)}$$

and

$$-1 \leqslant \mathcal{H}'(v_*^3) < 0. \quad \text{(A.29)}$$

Let us now consider the different cases of Appendix A.1.

1. If $\rho(v)$ is a non-monotonic function and there are three steady states [Fig. 7(d)], then:
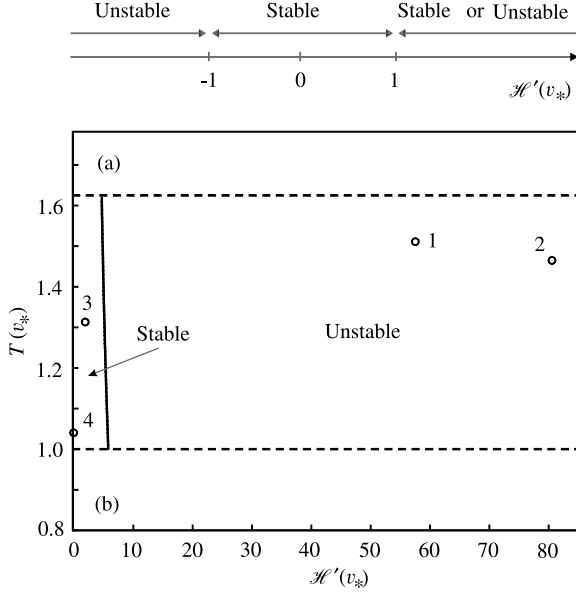
FIG. 11. Stability properties of the steady states. (a) A graphical representation of the content of Propositions 1 and 2 showing the dependence of the stability of a steady state on $\mathcal{H}'(T(v_*))$. (b) Bifurcation curve (A.36) for the rectangular distribution of delays (A.30); $T(v_*)$ is plotted vs. $\mathcal{H}'(T(v_*))$, for Γ from Table 1. For the (----) lines, $T(v_*) = T_{min} = 1$ and $T(v_*) = T_{max}$. (○ ○ ○ ○) Circles refer to the position of steady-states v_*^1 in the simulations shown Section 4.2; 1, Fig. 3; 2, Fig. 4; 3, Fig. 5; 4, Fig. 6.

(a) if v_*^1 satisfies Proposition 2 it is asymptotically stable. If not it can be asymptotically stable or unstable;

(b) v_*^2 is unstable according to eqn (A.28) and Proposition 1;

(c) v_*^3 is asymptotically stable according to eqn (A.29) and Proposition 2.

2. A unique steady-state v_*^1 [Fig. 7(b); for monotonic or non-monotonic $\rho(v)$] is asymptotically stable if it satisfies the requirement of Proposition 2. If not it can be asymptotically stable or unstable.

3. A unique steady-state v_*^3 [Fig. 7(f)] satisfies Proposition 2 and is therefore stable.

These statements are consistent with the results of our simulations in Section 4.2.

Further stability results can be obtained for special choices of the delay distribution $\bar{\xi}(T)$ only. Here we consider the rectangular distribution which was also used in the simulations.

A.2.1. Bifurcation Diagram for a Rectangular Density

Consider a distribution of delays with a rectangular density:

$$\bar{\xi}(T) = \begin{cases} 0 & 0 \leqslant T < 1, \\ \dfrac{1}{T_{max} - 1} & 1 \leqslant T \leqslant T_{max}, \\ 0 & T_{max} < T < \infty. \end{cases} \quad (A.30)$$

Functions employed in the stability analysis like $\mathcal{F}(v)$ and $\mathcal{H}'(v)$ can be easily evaluated for this case. (Figs. 7–10 were created using this rectangular density for the distribution of delays.)

For the stability analysis, we substitute the density (A.30) into eqn (A.19) and carry out the integration. Using (A.9) this yields

$$\lambda + \Gamma = -\Gamma \mathcal{H}'(v_*) \frac{e^{-\lambda T(v_*)} - e^{-\lambda T_{max}}}{\lambda(T_{max} - T(v_*))} \quad (A.31)$$

for $\theta_{min} \leqslant v_* \leqslant 1$, and

$$\lambda + \Gamma = -\Gamma \mathcal{H}'(v_*) \frac{e^{-\lambda} - e^{-\lambda T_{max}}}{\lambda(T_{max} - 1)} \quad (A.32)$$

for $v_* > 1$. In the following, we consider the case $\theta_{min} \leqslant v_* \leqslant 1$; the case $v_* > 1$ yields similar results. In eqn (A.31), we write $\lambda = \mu + i\omega$ and separate the real and imaginary parts. Since a stable fixed point v_* becomes unstable if it passes from negative μ through $\mu = 0$ to $\mu > 0$ we consider the set of points with $\mu = 0$. In this case the real and imaginary parts of (A.31) are

$$\omega^2 = \frac{2\Gamma \mathcal{H}'(v_*)}{T_{max} - T(v_*)} \sin \omega \frac{T_{max} + T(v_*)}{2} \times$$
$$\sin \omega \frac{T_{max} - T(v_*)}{2}, \quad (A.33)$$

$$\omega = \frac{-2\mathcal{H}'(v_*)}{T_{max} - T(v_*)} \cos \omega \frac{T_{max} + T(v_*)}{2} \times$$
$$\sin \omega \frac{T_{max} - T(v_*)}{2}. \quad (A.34)$$

Equations (A.33) and (A.34) yield an implicit equation for ω,

$$\Gamma \sin \omega \frac{T_{max} + T(v_*)}{2} + \omega \cos \omega \frac{T_{max} + T(v_*)}{2} = 0.$$

(A.35)

The solutions of (A.35) are the frequencies $\omega(\Gamma, T(v_*))$ which can be paired with $\mu = 0$. This equation has to be solved numerically. The solutions are subsequently inserted into (A.34) leading to values of $\mathcal{H}'(\Gamma, T(v_*))$ which allow for $\mu = 0$:

$\mathcal{H}'(T(v_*))$ from the stable side, the first passage through $\mu = 0$ marks the onset of instability; cf. Fig. 11(a). The transition happens for the smallest $\mathcal{H}'(T(v_*))$ of the set. The resulting bifurcation curve is shown in Fig. 11(b) for Γ chosen according to Table 1. Comparing these results with a state-independent density of delays, and a delta-function density for the delay distribution with a delay $\hat{T}$, shows that in the latter case the instability occurs at a value of $\mathcal{H}'(v_*)$ which corresponds to $\hat{T}$ equal to our T_{max}. This demonstrates the expected result that

$$\mathcal{H}'_*(\Gamma, T(v_*)) = -(T_{max} - T(v_*)) \frac{\Gamma \omega(\Gamma, T(v_*))}{2 \cos \omega (\Gamma, T(v_*))[T_{max} + T(v_*)]/2 \sin \omega (\Gamma, T(v_*))[T_{max} - T(v_*)]/2}.$$

(A.36)

Keeping Γ constant we find a set of solutions $\omega(T(v_*))$ of (A.35) and correspondingly a set of $\mathcal{H}'(T(v_*))$ from (A.36) where $\mu = 0$. Increasing

shorter delays stabilize the system: the stable regime in Fig. 11 is larger for smaller $T(v_*)$.